Coherent Phasic Excitation during Hippocampal Ripples

Nikolaus Maier,[1,10] Álvaro Tejero-Cantero,[3,4,10] Anja L. Dorrn,[1,2,5] Jochen Winterer,[1] Prateep S. Beed,[1] Genela Morris,[1,6,7] Richard Kempter,[6,8] James F.A. Poulet,[1,2,5,10] Christian Leibold,[3,9,10] and Dietmar Schmitz[1,2,5,6,10,*]
[1]Neurowissenschaftliches Forschungszentrum
[2]Cluster of Excellence NeuroCure
Charité-Universitätsmedizin Berlin, 10117 Berlin, Germany
[3]Division of Neurobiology, Ludwig-Maximilians-Universität München, 82152 Planegg, Germany
[4]Graduate School of Systemic Neurosciences, München, 82152 Planegg, Germany
[5]Department of Neuroscience, Max-Delbrück-Centrum für Molekulare Medizin (MDC), 13092 Berlin, Germany
[6]Bernstein Center for Computational Neuroscience Berlin, 10115 Berlin, Germany
[7]Department of Neurobiology and Ethology, Faculty of Science and Science Education, Haifa University, Haifa 31905, Israel
[8]Institute for Theoretical Biology, Humboldt-Universität zu Berlin, 10115 Berlin, Germany
[9]Bernstein Center for Computational Neuroscience Munich, 82152 Planegg, Germany
[10]These authors contributed equally to this work
*Correspondence: dietmar.schmitz@charite.de
DOI 10.1016/j.neuron.2011.08.016

SUMMARY

High-frequency hippocampal network oscillations, or "ripples," are thought to be involved in episodic memory. According to current theories, memory traces are represented by assemblies of principal neurons that are activated during ripple-associated network states. Here we performed in vivo and in vitro experiments to investigate the synaptic mechanisms during ripples. We discovered postsynaptic currents that are phase-locked to ripples and coherent among even distant CA1 pyramidal neurons. These fast currents are consistent with excitatory postsynaptic currents (EPSCs) as they are observed at the equilibrium potential of Cl⁻, and they display kinetics characteristic of EPSCs. Furthermore, they survived after intracellular blockade of GABAergic transmission and are effective to regulate the timing of action potentials. In addition, our data show a progressive synchronization of phasic excitation and inhibition during the course of ripples. Together, our results demonstrate the presence of phasic excitation during ripples reflecting an exquisite temporal coordination of assemblies of active pyramidal cells.

INTRODUCTION

Ripple oscillations in the hippocampal local field potential (LFP) of area CA1 have been described to occur during quiet wakefulness and slow-wave sleep (O'Keefe, 1976; O'Keefe and Nadel, 1978; Buzsáki, 1986; Buzsáki et al., 1992) and have taken center stage in current models of memory consolidation (Ego-Stengel and Wilson, 2010; Girardeau et al., 2009). These high-frequency

(~200 Hz) network oscillations commonly co-occur with large-amplitude sharp waves. The entire sharp-wave/ripple events (SWRs) represent ~40–150 ms periods of extensive activation of the hippocampo-subicular network (Buzsáki, 1986; Buzsáki et al., 1992; Ylinen et al., 1995). It has been demonstrated that assemblies of excitatory neurons coding for environmental trajectories are activated during SWRs before and after spatial experiences (Csicsvari et al., 2007; Dragoi and Tonegawa, 2011; Johnson and Redish, 2007; Karlsson and Frank, 2009; Kudrimoti et al., 1999; Lansink et al., 2009; Lee and Wilson, 2002; O'Neill et al., 2008; Wilson and McNaughton, 1994), and ripple-related phenomena were proposed to assist memory consolidation by stabilizing memory traces within the hippocampal network and in relaying them to target cortical areas (Axmacher et al., 2008; Buzsáki, 1989; Ji and Wilson, 2007; Siapas and Wilson, 1998; Wierzynski et al., 2009; for review, see Carr et al., 2011; Diekelmann and Born, 2010; Eichenbaum, 2000).

Although there is ample evidence for the involvement of ripples in mnemonic processes, the precise mechanisms underlying the generation of ripples are unclear. In search of the participating neuronal populations, in vivo studies mainly combined extracellular recordings with single-cell labeling to determine those classes of inhibitory interneurons that discharge during ripples (Jinno et al., 2007; Klausberger et al., 2003, 2004, 2005). It was shown that ripple activity is accompanied by an increased spiking probability in a subset of basket cells as well as bistratified and trilaminar interneurons. In contrast, discharge likelihood is reduced during ripples in oriens-lacunosum moleculare- and axo-axonic cells. These and previous studies (Csicsvari et al., 1999a; Ylinen et al., 1995) supported the idea that preferentially parvalbumin-positive basket neurons, which exert a powerful inhibitory control over the pyramidal cell soma, shape ripple oscillations during a transient excitatory input that accompanies SWRs. By contrast, alternative mechanisms of ripple generation have been put forward wherein electrical coupling (Draguhn et al., 1998; Traub et al., 1999) or combined mechanisms involving synaptic end electrical

coupling (Traub and Bibbig, 2000) contribute to the oscillogenesis. In these models, the phasic discharge of assemblies of pyramidal neurons are the immediate source of ripples (Leibold and Kempter, 2006). A straightforward prediction of such a synchronous activation of pyramidal cells during ripples would be the presence of phasic excitation that is coherent across the neuronal network and apparent as excitatory postsynaptic currents (EPSCs) and potentials at the single-cell level.

In the present study, we investigated synaptic input onto CA1 pyramidal cells during ripples, combining in vivo and in vitro electrophysiology. We identified phasic excitatory postsynaptic currents that were locked to field ripples and coherent among pairs of principal cells. In addition, we characterized SWR-locked inhibitory currents to determine their timing in relation to phasic excitatory currents during ripples.

RESULTS

To directly study synaptic inputs onto CA1 pyramidal neurons during SWRs in vivo, without confounding effects of anesthesia, we used a recently established approach where mice were habituated to head restraint in the recording setup over several days (Crochet and Petersen, 2006; Harvey et al., 2009; Margrie et al., 2002). During quiet wakefulness, LFP recordings in the area CA1 revealed SWRs comparable to those observed in chronically implanted animals (e.g., Buzsáki et al., 2003; Figures 1A–1E). On average, in 16 mice, SWR incidence was 0.14 ± 0.02 Hz (median: 0.15 Hz; range: 0.02 Hz to 0.29 Hz), the mean ripple oscillation frequency was 136.3 ± 1.6 Hz (median: 137.0 Hz; range: 127.0 Hz to 147.0 Hz; n = 1,288 events), and mean ripple duration was 65.0 ± 0.7 ms (median: 60.9 ms; range: 12.1 ms to 156.6 ms; Figure S1A available online). Next, we combined LFP recordings with simultaneous whole-cell recordings and stainings from nearby CA1 pyramidal neurons (Figure 1F). Out of a total number of 19 cells, 6 neurons were successfully stained, and they revealed the typical morphology of CA1 principal cells (see Figures 1F and 1H). Whole-cell recordings during ripples revealed a membrane potential depolarization followed by hyperpolarization (Figure S1B). Synaptic input during SWRs was frequently superimposed with fast ripple-associated voltage fluctuations (see Figures 1F and 1G; n = 241 events from 12 cells). When we clamped cells at a voltage close to the reversal potential of Cl⁻ (−70 mV), we observed ripple-associated inward currents. Figures 1H and 1I display example traces and the average of postsynaptic currents (PSCs) during extracellular SWRs (n = 421 events from 8 cells). Experimental drawbacks complicate the biophysical interpretation of in vivo whole-cell voltage-clamp data: To precisely determine the contribution of excitation during SWRs at the single-cell level, it is necessary to clamp a cell's voltage at the equilibrium potential of Cl⁻, which requires exact knowledge of the extracellular ion concentrations. Second, owing to the often high series resistance of in vivo recordings (Lee et al., 2006; Margrie et al., 2002) and voltage-clamp errors (Williams and Mitchell, 2008), both the polarity and the timing of fast synaptic currents, in particular if they arise from distal synapses, are difficult to determine.

We therefore turned to a previously established in vitro model of hippocampal SWRs (Maier et al., 2009; schematic, Figure 2A).

There, sharp waves occur spontaneously at a rate of 0.77 ± 0.05 Hz (n = 28 slices), and their associated ~200 Hz ripples are similar to the in vivo phenomenon with respect to oscillation frequency, region of origin, laminar depth profile, and propagation through the hippocampal network (Buzsáki, 1986). We used the in vitro approach to characterize currents in single principal cells of area CA1 while simultaneously sampling the LFP at close-by recording sites (Figure 2A). We observed large-amplitude PSCs in temporal alignment with the extracellular SWRs. Closer inspection revealed compound bursts of postsynaptic currents (cPSCs; Figure 2B) with a distinct frequency at ~200 Hz matching the dominating frequency of LFP ripples (Figures 2A, bottom and 2C). Peak ripple frequencies ranged between 160 and 240 Hz, with an average of 194 ± 6 Hz (n = 1,137 SWRs from 15 cells; Figure 2D). A similar frequency component was observed for postsynaptic potentials in the current-clamp configuration (Figure S2). To quantify the relationship between cPSC bursts and field ripple oscillations, we determined their coherence. In eight simultaneous whole-cell/LFP recordings, we observed a peak of coherence at ~200 Hz (Figure 2E).

To demonstrate the synchrony of inputs in cells constituting the local network, we examined how the observed single-cell-to-ripple coherence extends to the network level (see Figure S3A for extracellular ripple coherence). If ripple-locked cPSCs indeed represent signatures of neuronal population oscillations, we would expect a synchrony of inputs across multiple cells in the local network, and cell-to-cell input coherence should extend over a considerable distance. We tested this hypothesis in 20 dual pyramidal cell recordings (Figures 3A and 3B; 2,132 SWR-associated cPSCs were analyzed). Consistent with inputs from a synchronized network during SWRs, cPSCs were correlated, as determined by cross-correlation analysis (Figure 3C). The amplitudes of cross-correlation peaks decreased with distance, and their time lags increased (Figures 3D and 3E; n = 20 dual cell recordings analyzed). Both observations are in agreement with a spread of SWR activity from proximal to distal sites in CA1 with respect to CA3. In addition, we found that ripple-associated cPSCs in pairs of pyramidal neurons were phase coherent, as demonstrated by coherence maxima in the ripple frequency range (Figure 3F). Cell-to-cell coherence maxima of cPSCs insignificantly decreased with increased spatial separation between cells (Figure 3G; R = −0.26, p = 0.26). In line, comparison of cPSC coherence in close (<100 μm apart) versus distant (450–580 μm) neuron pairs revealed no significant difference (Figure 3H; p = 0.39; rank-sum test). Together, these results on dual principal cell recordings confirm that ripple-locked cPSCs are indeed signatures of population oscillations.

From the above experiments, it is not clear whether the observed synchrony is mediated by excitation, inhibition, or both (Figure S3B). To differentiate, we recorded from principal neurons at −66 mV, close to the reversal potential of Cl⁻ (−67 mV in our conditions). By choosing this holding potential, we considerably reduced the driving force for Cl⁻ and hence Cl⁻-driven GABA_AR-mediated inhibition (see Figure S4A for the experimental confirmation of the Nernst potential). The kinetics derived from spontaneous EPSCs (not associated with ripples) were fast enough to account for excitatory currents in
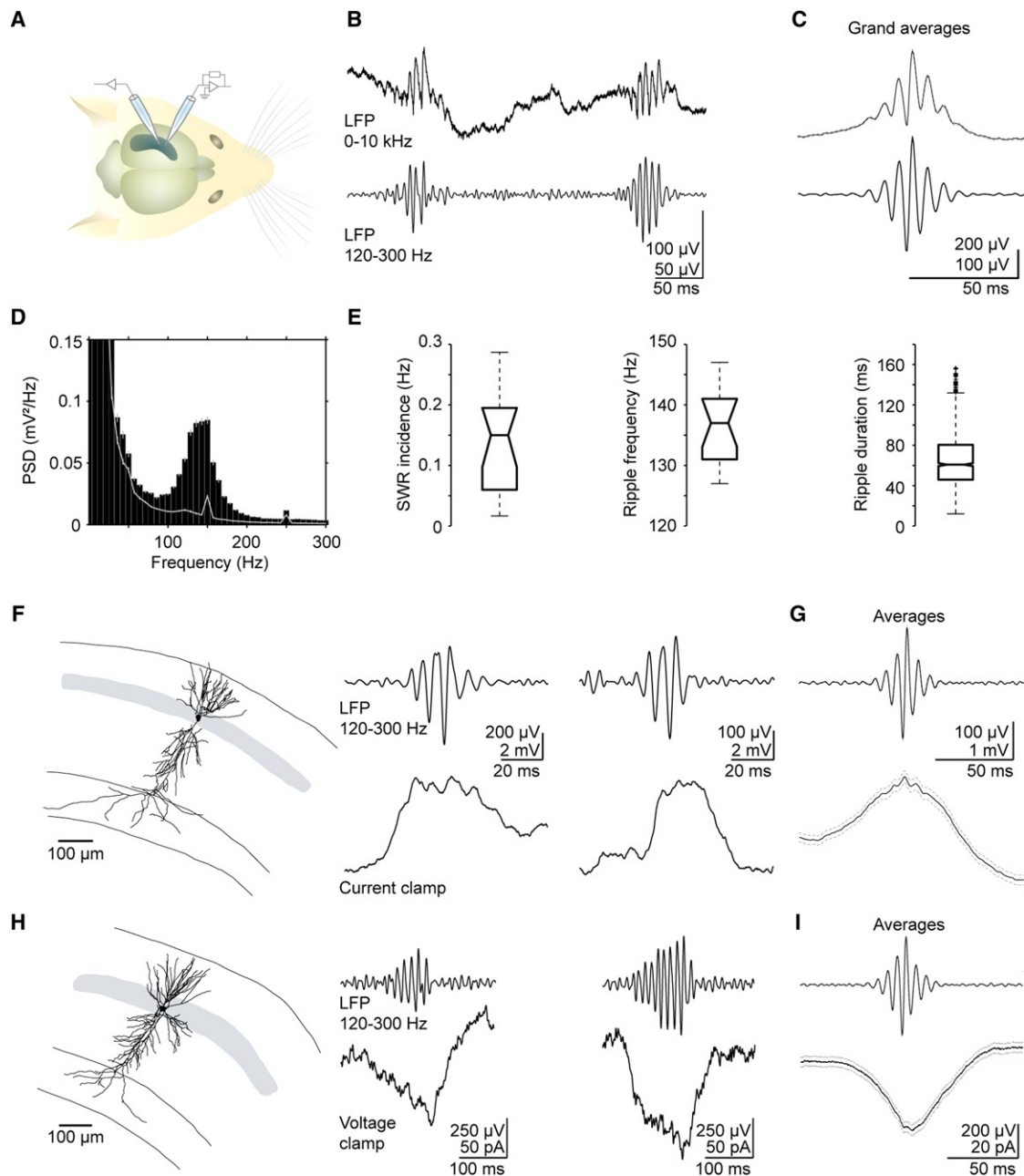
Figure 1. Intracellular Recordings from CA1 Pyramidal Neurons during LFP Ripples in Head-Fixed, Awake Mice

(A) Schematic of the recording configuration.

(B) Unfiltered extracellular recording of SWRs in area CA1 (top) and 120–300 Hz bandpass-filtered version (below).

(C) Grand averages (±SEM, dashed) of 1,288 SWR events from 16 mice.

(D) Average power spectral density (PSD) of all identified ripples and of eventless epochs preceding ripples (gray line).

(E) Statistics of SWR incidence, ripple peak frequency, and duration from all recorded animals (n = 16 mice).

(F) Left: Anatomical reconstruction of a CA1 pyramidal cell. Right panels: Ripple-associated current-clamp data from this cell (bottom) and simultaneously recorded LFP (top).

(G) Averages (±SEM, dashed) of 241 membrane potential traces (bottom) during ripples (top; 12 cells from 10 mice). Note preserved ripple signature in the average of the intracellular signal.

(H) Left: Anatomical reconstruction of a CA1 pyramidal neuron in a different animal than that in (F). Right panels: Ripple-associated voltage-clamp data and the simultaneously recorded LFP. Holding potential was close to the cell's resting membrane potential (−70 mV).

(I) Averages (±SEM, dashed) of 421 postsynaptic current traces (bottom) during LFP ripples (top; 8 cells from 5 mice).

See also Figure S1.
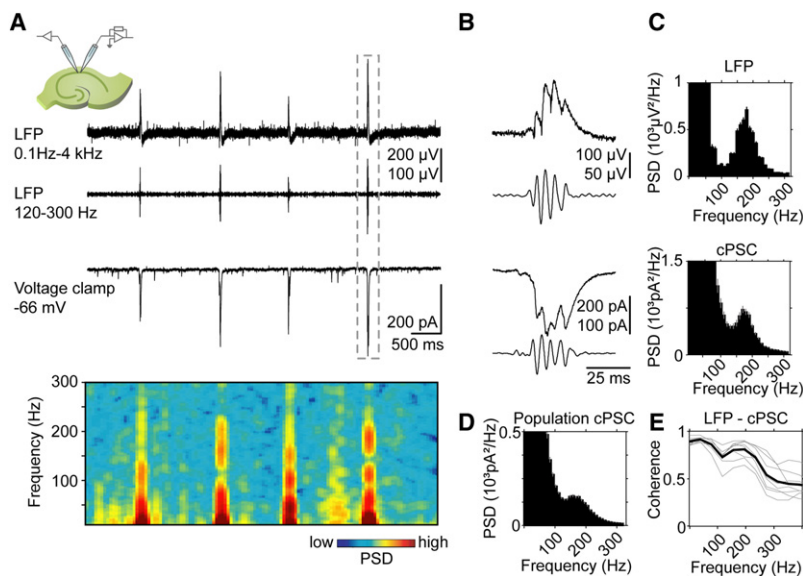
Figure 2. Phasic Postsynaptic Currents in CA1 Pyramidal Neurons during LFP Ripples In Vitro

(A) In hippocampal slices, extracellular recordings were combined with close-by patch-clamp recordings from CA1 pyramidal cells (schematic, top left). Top trace: Extracellular SWRs in CA1, filtered version (as indicated, middle), and simultaneously recorded PSCs (below; cell clamped at −66 mV). Note the co-occurrence of LFP ripples and compound PSCs. Bottom: Spectrogram of the voltage-clamp current trace shown above. Periods of enhanced power at ∼120–250 Hz coincide with ripple-associated PSCs.

(B) Magnification of the boxed SWR in (A) and its corresponding cPSC. Respective 120–300 Hz filtered versions are shown below.

(C) Averaged power spectral densities (133 individual spectra) of the LFP signal (top) and respective cPSCs (bottom) from the recording in (A); both spectra show a distinct component at ∼200 Hz.

(D) Average PSD of 1,137 PSC segments during ripples (15 cells) peaks at ∼195 Hz.

(E) Coherence between LFP and cPSC signals peaks at ripple frequency (∼200 Hz; 8 slices).

See also Figure S2.

ripple-associated cPSCs (Figure 4A). To corroborate this hypothesis, we quantified the temporal structure of ripple-coherent cPSCs. The underlying assumption was that rise times of synaptic currents are faster than their decays. At potentials below the reversal potential of excitatory synaptic transmission, *excitatory* currents within cPSCs are inward and should thus display downward slopes (rises) steeper than their upward slopes (decays). In addition, at the potential we have chosen, putative inhibitory outward currents should display only small amplitudes, due to the small driving force for Cl⁻. We analyzed the slopes within cPSCs in eight cells recorded at −66 mV (1,085 cPSCs in total). In line with EPSC kinetics, we found that downward slopes were indeed steeper than upward slopes (Figure 4B): The analysis revealed slope values of 35.7 ± 0.5 pA/ms versus 18.9 ± 0.2 pA/ms for the populations of 10% strongest downward and upward slopes in individual cPSCs (p = $1.6 \cdot 10^{-178}$; Kolmogorov-Smirnov test [K-S test]; n = 8 cells). We further checked whether the interval distribution of strong downward slopes can be related to ripples. Indeed, the incidence of strong downward slopes was in the range of ripple frequency as demonstrated by a peak at ∼5 ms in interdownward slope-interval histograms (Figure 4C; see Figure S4B for single-cell analysis). Based on these findings, we hypothesized that the putatively excitatory PSCs are locked to the LFP. In this case, the oscillatory structure in the LFP should be revealed by the strong downward slopes in cPSCs, and the downward slope phase relative to LFP ripples should be constant across cells. To test both assumptions, we computed 40 ms averages of LFP signal centered on onsets of PSC downward slopes and examined the distribution of PSC slope phases. Indeed, slope-triggered LFP averages were rhythmically modulated at ∼5 ms (Figure 4D), and slope phases were largely constant (Figure 4E, inset), both indicating that downward slopes are consistently phase-locked to ripple oscillations (n = 8 parallel LFP/cell recordings).

The slope analysis within cPSCs recorded close to the Cl⁻ reversal potential, however, does not unequivocally reveal whether ripple-locked cPSCs can be explained by phasic excitation alone, or whether they reflect a slow transient increase of excitation superimposed with fast inhibitory PSCs (schematic, Figure S3B). To add further evidence in support of our hypothesis, we developed a fitting algorithm to reconstruct the current traces using a mathematical model that assumes a linear superposition of only excitatory (inward) PSCs. This reconstruction was done iteratively by fitting PSCs of the SWR-associated current trace (Figures 5A and S5A; see also Supplemental Experimental Procedures). As fit parameters we used PSC amplitude, onset time, as well as rise and decay time constants. The distributions of fit parameters (Figure 5C) were in line with (1) statistics of spontaneous PSCs (Figure S5C, red), (2) interdownward slope intervals (Figures 4C and 5C), (3) slope-to-LFP locking (not shown), and (4) the mean cPSC (Figure 5B, grey). Finally (5), distributions of fit parameters were similar across cells (Figure 5C). The reconstructions thus show that the shapes of cPSCs are consistent with the assumption of currents exclusively composed of excitatory components.

To further experimentally corroborate our hypothesis of the existence of ripple-coherent excitatory PSCs, we sought to directly investigate excitation during ripples by blocking inhibition. Bath application of antagonists at GABA_A receptors is experimentally inappropriate because they not only block inhibitory PSCs but also disrupt SWRs as a collective network phenomenon (Ellender et al., 2010; Maier et al., 2003; Nimmrich et al., 2005). We therefore blocked GABAergic synaptic inputs at the single-cell level by applying 4,4′-diisothiocyanostilbene-2,2′-disulfonic acid (CsF-DIDS; Nelson et al., 1994). To demonstrate the reliability of this tool, we first recorded currents mediated by UV-flash-triggered photolysis of "caged" GABA with control intracellular solution (see Experimental Procedures). Following repatching of the same cells with CsF-DIDS and repeated "uncaging" of GABA, we indeed observed blockade of postsynaptic GABA currents (Figure 6A). Likewise, we successfully blocked inhibitory PSCs evoked by stimulation of inhibitory
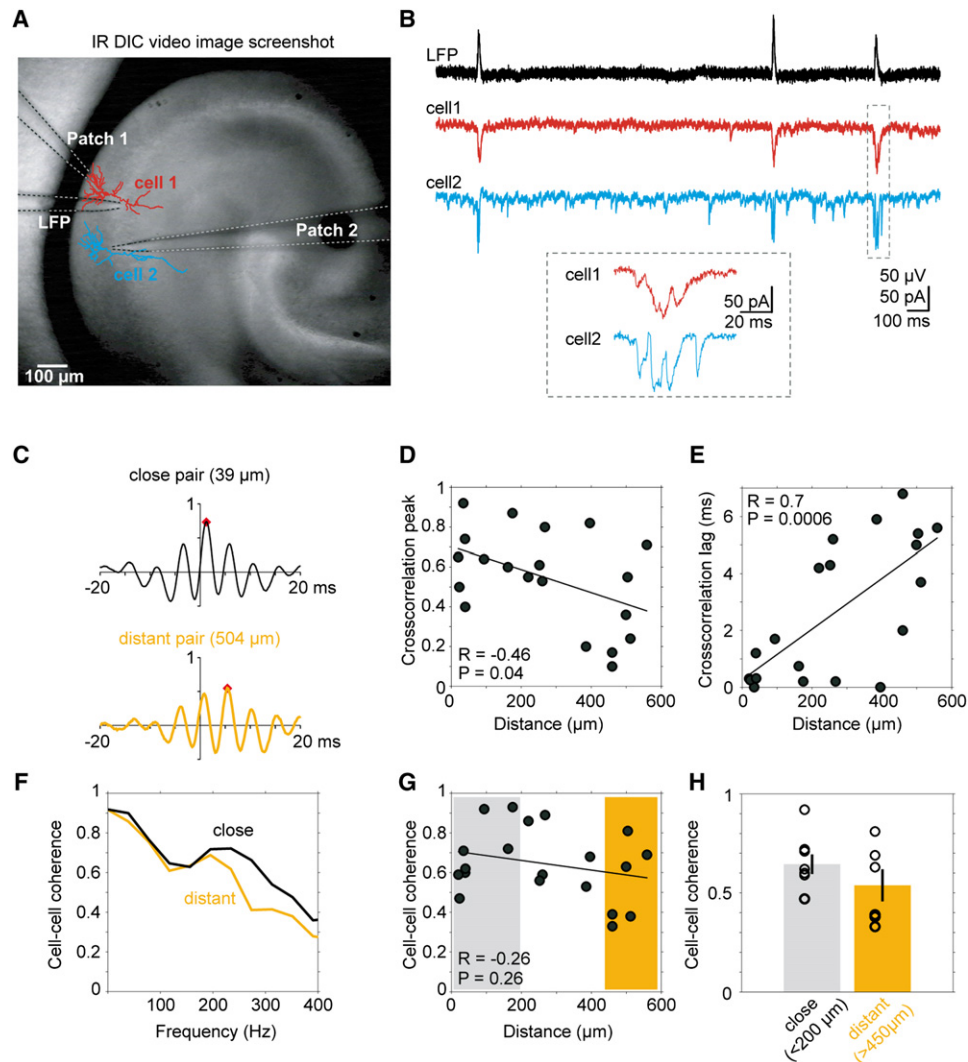
Figure 3. Coherence of cPSCs across Simultaneously Recorded Principal Cells during Ripples

(A) Reconstructions of pyramidal cells (blue and red) projected on an infrared differential interference-contrast (IR DIC) video image screenshot. *LFP*, *Patch 1*, and *Patch 2* indicate the electrodes' arrangement.

(B) Simultaneous recording from both cells and LFP of the experiment demonstrated in (A). The inset represents a magnification of the boxed events.

(C) Correlation analyses of two example recordings at different cell distances. Top: Cross-correlation function of cPSCs in two adjacent cells. Correlation peak (red mark) and lag: 0.74 and 1.2 ms, respectively. Bottom: Cross-correlation function of cPSCs in two distant cells. Correlation peak (red mark) and lag: 0.55 and 5.4 ms.

(D) The peak correlation decreases as a function of distance between recorded neurons (n = 20 simultaneous recordings; $R = -0.46$; p = 0.04). Cells located in proximal CA1 were taken as reference.

(E) The peak time lag increases with distance between recorded neurons (n = 20 simultaneous recordings; R = 0.7; p = 0.0006).

(F) CPSC coherence functions from close versus distant dual recordings (same pairs as in C).

(G) Peak coherence values in the 120–300 Hz range as a function of distance within CA1. Linear regression reveals a modest negative correlation (n = 20 simultaneous recordings; $R = -0.26$; p = 0.26).

(H) Mean peak coherence values in close (<200 μm) and distant (>450 μm) recordings are similar (colors as in G; peak coherences: close: 0.65 ± 0.05; n = 8; distant: 0.54 ± 0.08; mean ± SEM; n = 6; p = 0.41; Mann-Whitney test).

See also Figure S3.

fibers after repatching cells with CsF-DIDS (Figures 6B and S6A). Subsequently, we used this approach to test our hypothesis of oscillation-locked excitatory inputs during ripples. We applied CsF-DIDS in repatches of seven cells after having collected a sufficient number of ripple-associated cPSCs under control conditions close to the potential of Cl⁻ reversal. In line with our hypothesis, ripple-associated fast synaptic inputs indeed persisted in the repatch recording with disrupted GABA$_A$R-mediated synaptic transmission (Figure 6C). We again analyzed downward and upward slopes of putative EPSCs and compared
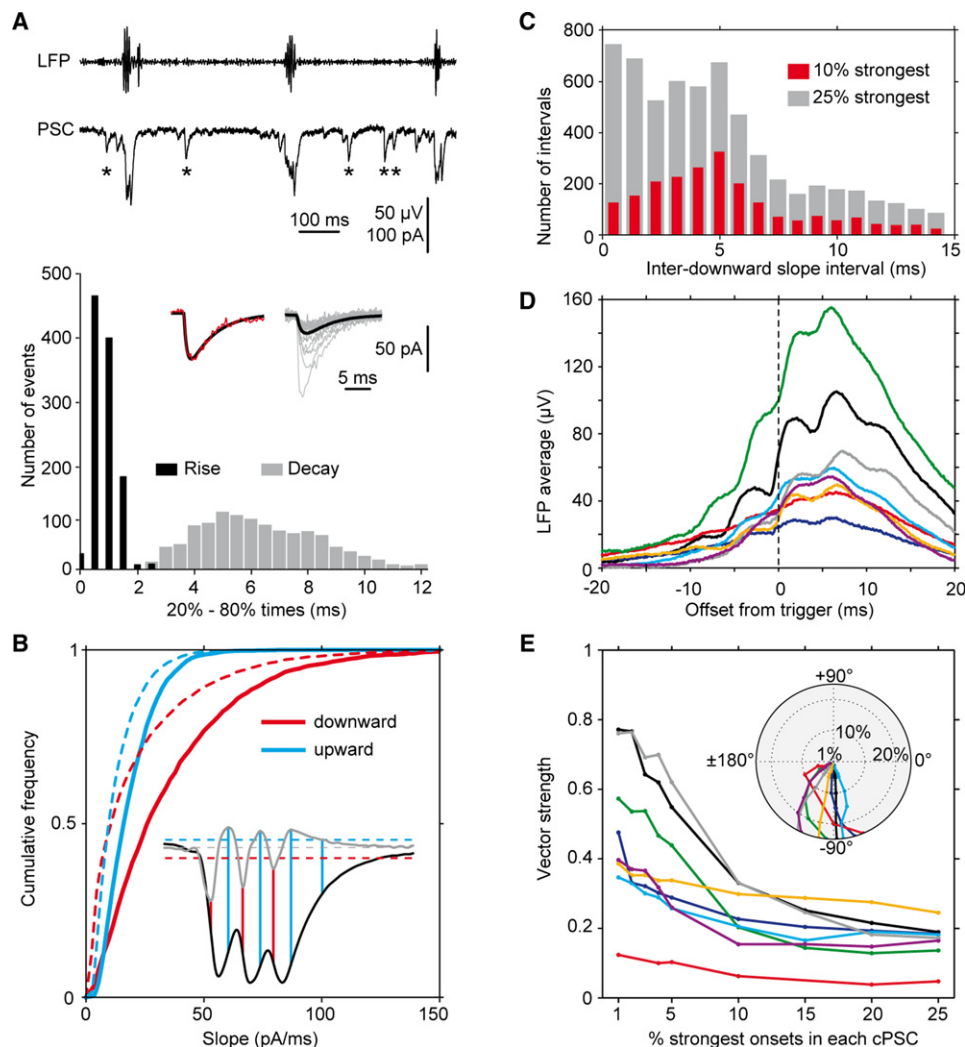
Figure 4. Slope Analysis of Postsynaptic Currents

(A) In eight simultaneous LFP (top) and whole-cell voltage-clamp recordings (bottom, recorded at −66 mV), spontaneous, non-ripple-associated PSCs as those marked by asterisks in the lower trace were extracted. Histograms display 20%–80% rise and 80%–20% decay times of these non-ripple PSCs (0.83 ± 0.01 ms and 6.66 ± 0.09 ms). Left inset: To determine rise and decay times of a PSC (red), an alpha function (black) was fitted; right inset: example PSCs (gray) and average (black).

(B) For ripple-associated cPSCs, we identified cumulative distributions of downward and upward slopes. Distributions reflect the population of 10% (solid) and 25% (dashed) strongest slopes of all cPSCs (10%: 35.7 ± 0.5 pA/ms and 18.9 ± 0.2 pA/ms; 25%, dashed line: 21.1 ± 0.3 pA/ms and 13.1 ± 0.1 pA/ms, for downward and upward slopes). The inset exemplifies the detection of slopes (10% strongest) in cPSCs. The value of the derivative (gray) of the 400 Hz low-pass-filtered current trace (black) is compared to the 10% threshold levels of steepest slopes (dashed blue: upward; dashed red: downward). Vertical lines mark the times of identified slopes.

(C) Distributions of interdownward slope intervals of the two populations of analyzed slopes (color-coded). Both distributions peak at 5 ms, indicating ripple frequency modulation.

(D) Putative EPSCs lock to LFP ripples, as demonstrated by averaging 40 ms LFP data stretches centered on the times of the 10% steepest downward slopes of each cPSC (colors identify the eight different cells).

(E) Vector strength of downward slopes versus fraction of strongest slopes (in respective individual cPSCs), indicating significant locking to ripple phase (p < 0.05; Rayleigh test) almost independent of the fraction of slopes taken into account. Colors identify individual experiments as shown in (D). Inset: Polar plot of mean phases of putative EPSCs for the eight experiments (colors) versus fraction of strongest slopes. The mean phase (over cells) at 10% threshold of strongest slopes is −114° ± 10°, corresponding to putative EPSCs leading the LFP ripple peak by ∼1.5 ms on average.

See also Figure S4.

their values before and following perfusion of the cells with CsF-DIDS. Moreover, ripple-locked downward cPSC slopes were unchanged following intracellular block of inhibition (control: 24.3 ± 0.8 pA/ms, n = 224 cPSCs; CsF-DIDS: 26.6 ± 0.7 pA/ms, n = 462 cPSCs; 7 repatched cells; p = 0.1; K-S test), whereas upward slopes were slightly enhanced (control: 12.9 ± 0.3 pA/ms; CsF-DIDS: 13.9 ± 0.2 pA/ms; Figure 6D; p < 0.0001; K-S test). Additionally, we examined the intervals
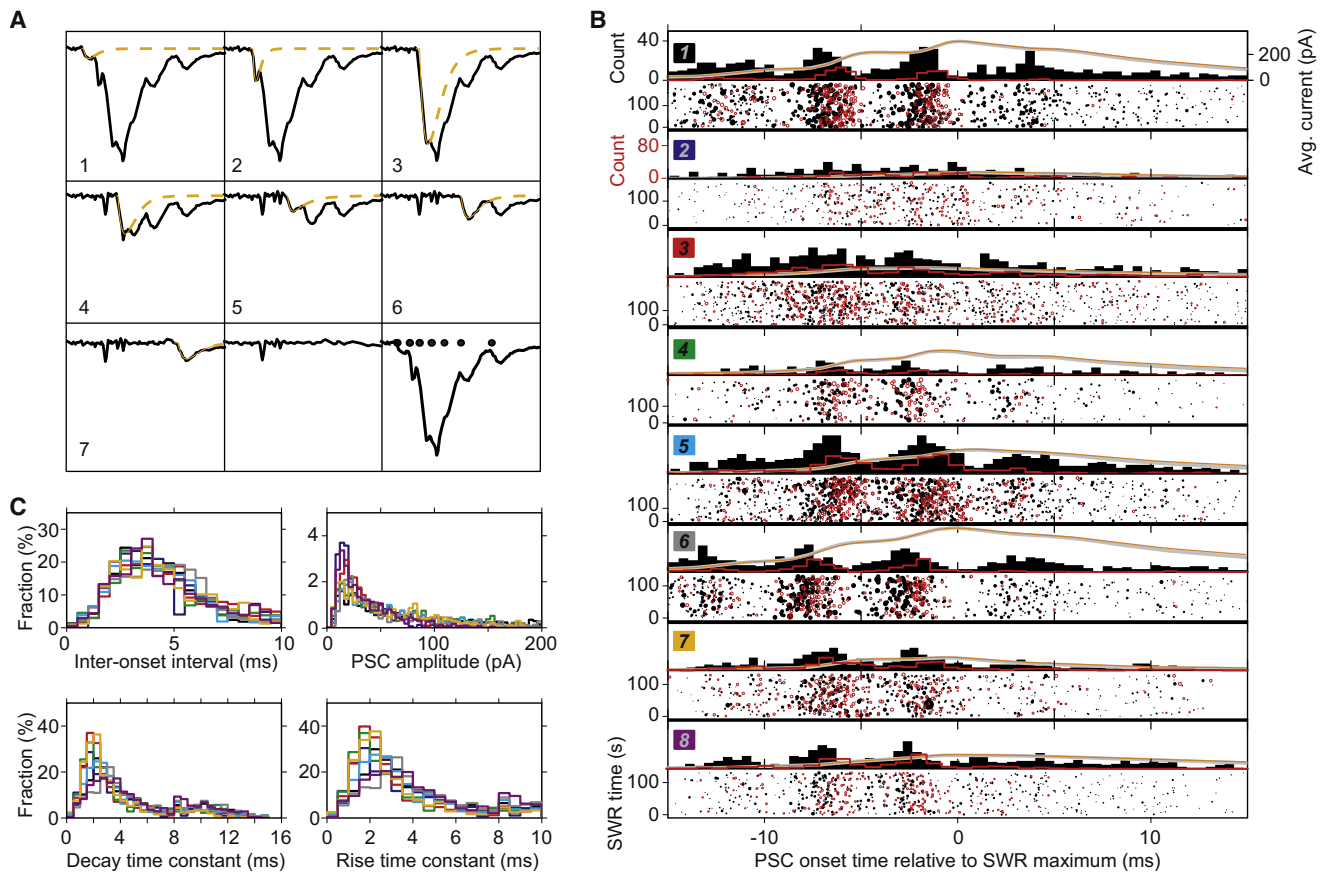
Figure 5. Reconstruction of cPSCs by a Superposition of Inward Currents

(A) Example trace to illustrate iterative peeling reconstruction algorithm (see also Supplemental Experimental Procedures). In each panel the leftmost PSC is fitted by a model function (dashed yellow) and subtracted from the trace. In the shown example, seven PSCs could be fitted. The residual (middle bottom) displays the fitting error consisting of only high-frequency components indicative of the limits of the model function. The final fit (bottom right) reveals the putative fitted onsets of the PSCs (black dots).

(B) Summary of the peeling reconstruction analysis. Color squares and numbers (upper left corners) label the eight cells analyzed; colors as in Figures 4D and 4E. Black histograms and dot-raster plots represent PSC onset times and amplitudes as obtained from the reconstruction. Red histograms and dot-raster plots demonstrate PSC 10% steepest downward slopes taken as proxies of PSC onsets for the analysis of rhythmicity (as in Figure 4C) and locking (Figures 4D and 4E). Dot sizes are proportional to fitted amplitude and slope strength. Note the shift of the strong slopes compared to the fitted onsets (red versus black) due to the time it takes the EPSC slope to reach detection threshold. Inverted cell-average cPSCs (grey) have been plotted on top of the inverted average reconstructions (orange) to illustrate the goodness of fit at a population level. Y axis calibrations: For dot-raster plots, the time of SWRs in the individual experiments is indicated (bottom left); for histograms, event counts are displayed (black and red); cPSC averages and reconstructions are scaled as indicated at top right.

(C) Histograms of inter-onset intervals and fit parameters for individual component PSCs embedded in cPSCs for all eight cells from (B) (identical colors). See also Figure S5.

between successive downward slopes. Distributions peaked at 4–5 ms, consistent with ripple frequency, both in control conditions and after CsF-DIDS administration (Figure 6E; see Figure S6B for single-cell data). Taken together, these results derived from experimentally blocking the somatic postsynaptic action of GABAergic inputs corroborate our hypothesis that ripples are accompanied by a strong oscillation-coherent phasic excitatory component.

We next asked whether ripple-coherent cPSCs represent the spiking output of CA3 pyramidal neurons (Both et al., 2008) or whether they are generated locally within the CA1 network. We used "minislices" where area CA1 was isolated from the adjacent CA3 and subiculum (Figures 7A and 7C). In this experimental

system, we observed SWRs at a rate of 0.46 ± 0.09 Hz (median: 0.46 Hz; range: 0.13 Hz to 0.93 Hz; 8 CA1 minislices; Figure 7B). Ripple frequency in these events was 213.1 ± 6.6 Hz on average (median: 215 Hz; range: 175 Hz to 235 Hz; Figure 7B, right). To test whether ripple-coherent cPSCs survived in the isolated area CA1, we again recorded from principal neurons voltage-clamped close to the reversal potential of Cl^- (-66 mV). SWRs in CA1 minislices were indeed accompanied by phasic inward currents at ripple frequency that were also phase coherent with LFP ripples (Figures 7D–7E; n = 725 cPSCs; 5 cells). Moreover, in minislices, cPSC downward slope phases with respect to LFP ripples ($-101° \pm 8°$, Figure 7F) were comparable with those derived from intact slices ($-114° \pm 10°$, Figure 4E). In summary,
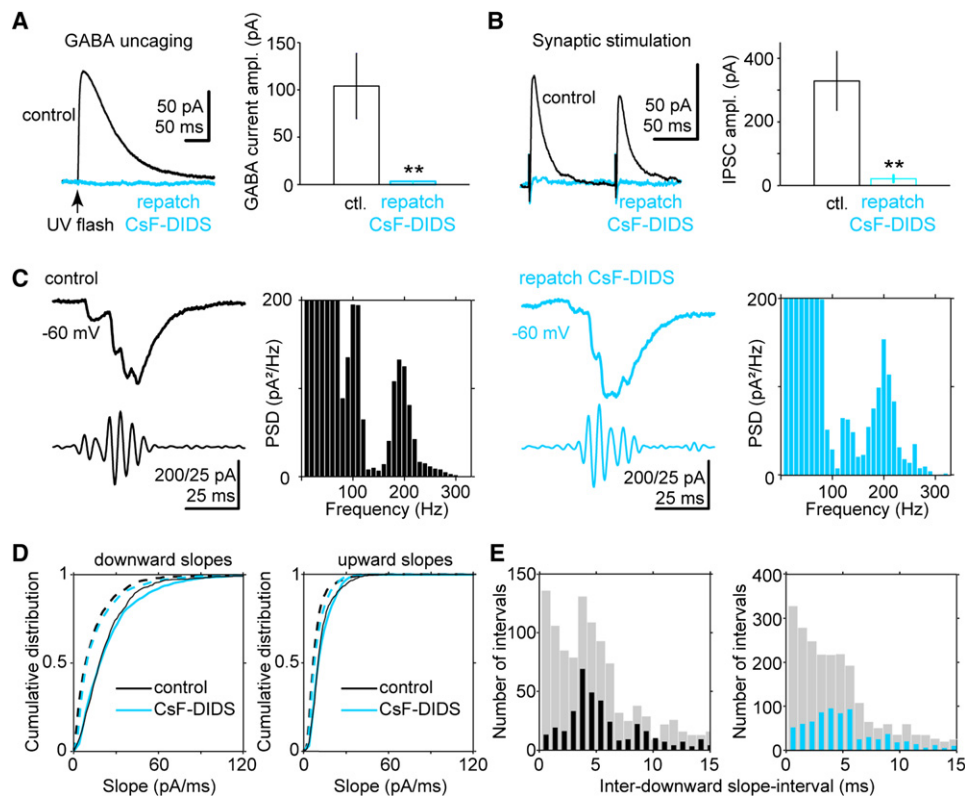
Figure 6. Intracellular Blockade of Inhibition Reveals Strong Excitatory Contribution to Phasic Ripple-Associated cPSCs

(A) Postsynaptic current after GABA uncaging by a brief UV flash without (black; control) and with intracellular blockade of inhibition (blue; 1 mM CsF-DIDS perfusion; 10 μM NBQX; and 50 μM D-APV in extracellular medium; holding potential, -59 mV). Control: 104 ± 34 pA; repatch: 3.2 ± 1.3 pA (mean $\pm$ SEM; n = 5; p = 0.008; rank-sum test).

(B) Stimulus-evoked IPSCs are blocked after intracellular perfusion with CsF-DIDS. Control: 329 ± 95 pA; repatch: 21 ± 11 pA (mean $\pm$ SEM; n = 6; p = 0.002; rank-sum test). Cells were clamped at -59 mV.

(C) Ripple-associated PSCs in CA1 principal cells remain stable (>15 min) following intracellular blockade of inhibition. Upper traces: cPSCs in control (black) and repatched with CsF-DIDS (blue). Bottom: 120–300 Hz bandpass-filtered cPSCs. Right panels: PSDs of the displayed traces.

(D) Cumulative distributions of downward and upward slopes detected in cPSCs in control (black) and after CsF-DIDS perfusion (blue). Distributions reflect the populations of 10% (solid) and 25% (dashed) strongest slopes within a given cPSC.

(E) Interdownward slope intervals detected in cPSCs in control (left; 7.4 ± 0.2 ms; mean $\pm$ SEM; for 10% strongest slopes) and CsF-DIDS (right; 6.3 ± 0.1 ms; for 10% strongest slopes). Gray histograms represent 25%, whereas black and blue reflect the subset of 10% strongest intervals in individual cPSCs. The overall number of intervals was smaller in control recordings as these were kept short to increase the success rate of the repatch with Cs-DIDS.

See also Figure S6.

this set of experiments demonstrates the possibility of a local origin of ripple-coherent excitatory PSCs within area CA1.

The observation that excitatory PSCs are phasic and ripple-locked raised the question of whether they could account for the timing of action potentials in target CA1 principal neurons. We investigated this using three approaches: We analyzed action potential timing both during injection of synthetic cPSCs and during SWRs and found that spikes are significantly phase-locked to the ripple component (Figure S7). To further substantiate this finding, we also analyzed action potential timing during blockade of inhibition at the single-cell level. To do so, we applied DNDS, which blocks GABA$_A$R-mediated inhibition from the intracellular side without changing action potential firing (Dudek and Friedlander, 1996) (Figure 8). Using this approach we found that action potentials were locked to ripples (spike-time histograms in Figures 8F and 8H;

log$_{10}$ p values in the range of -54.3 and -1.6; n = 1,119 spikes associated with 1,564 SWRs; 7 cells). Together, these experiments demonstrate that the ripple-locked excitatory inputs remaining after block of inhibition can effectively regulate the spike timing of target principal neurons.

In a final set of experiments, we studied the timing of ripple-associated inhibition relative to phasic excitation during SWRs. At the excitatory reversal potential (~-6 mV; Figure S8), we observed complex outward currents reflecting the superposed inhibitory inputs present during ripples (Figures 9A and 9B). These currents were also significantly locked to ripples, as demonstrated by onset phase analysis, onset-triggered LFP averaging, and peeling reconstruction analysis (Figures 9C–9E; n = 849 events in 6 cells). We compared the timing of phasic excitation and inhibition, as derived from cEPSC and cIPSC slope onsets and peeling reconstruction. Figure 9E juxtaposes the
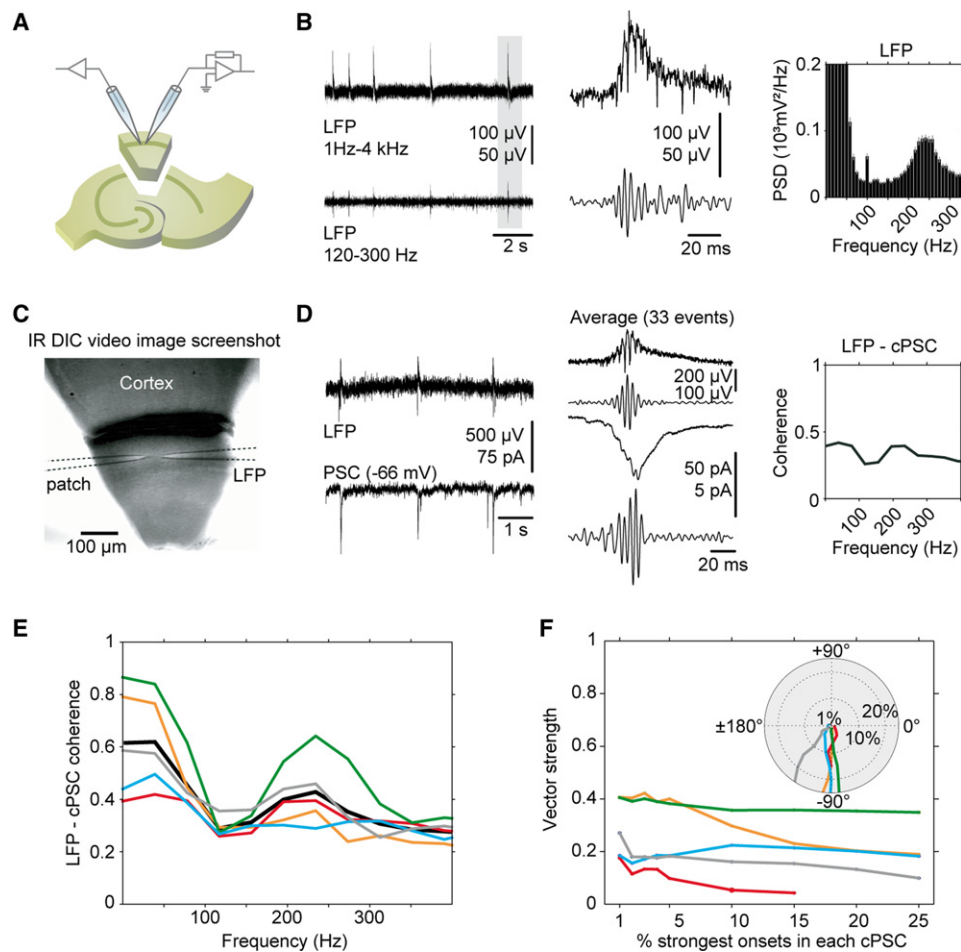
**Figure 7. Ripple-Coherent Excitatory Currents Persist in CA1 Minislices**
(A) Schematic of the CA1 minislice approach.
(B) Left: CA1 minislices do generate SWRs at slow pace. Top: SWRs recorded in *stratum pyramidale*. Bottom: Filtered version of the above, as indicated. Middle: The event marked gray shown at higher resolution. Right: Averaged PSD plot from this experiment (153 individual spectra). Note the peak at ripple frequency.
(C) Left: In a different CA1 minislice, PSCs were recorded from a principal neuron in parallel with the LFP. The video image screenshot shows the CA1 minislice and the electrode arrangement.
(D) Left: Example LFP-SWRs and associated PSCs. Middle: 33 LFP and PSC events (1st and 3rd from top) were averaged triggered on the LFP ripple maximum. Respective filtered versions below. Right: Coherence analysis of LFP and cPSC data from this experiment reveals a peak at ripple frequency (∼200 Hz).
(E) Population analysis of five minislice experiments (individual coherence functions in colors and average in black).
(F) Vector strength of downward slopes versus fraction of strongest slopes in respective individual cPSCs, indicating significant locking to ripple phase (p < 0.05; Rayleigh test). Inset: Polar plot of mean phases of putative EPSCs for the five experiments versus fraction of strongest slopes (colors as in E). Note that the mean phase (−101° ± 8°) is comparable to that of cPSCs recorded in full slices (see Figure 4E).

dynamics of ripple-locked excitatory and inhibitory currents for two cells, and Figure 9F summarizes the averaged fitted onset histograms for 8 and 6 cells, respectively. During the initial course of ripples, excitation is slightly phase-advanced, leading inhibition by ∼1.5 ms. In later periods, the phases of the two components converge (phase difference plot in Figure 9F, black line). This finding is confirmed by comparing the lags of correlation peaks determined for 48 excitatory-inhibitory cell pairs early versus late in the ripple (Figure 9G). Cross-correlation peaks computed on the earlier period, between −16 and 0 ms relative to the SWR peak, clustered around −2 ms (median: −2.0 ms; blue histogram), whereas those computed between

0 and +16 ms clustered around 0 ms (median: 0 ms; green histogram). Together, these analyses reveal high precision of ripple-associated inputs and a progressive synchronization of excitation and inhibition during the course of ripples.

DISCUSSION

Here, we combined an in vivo approach (Crochet and Petersen, 2006; Margrie et al., 2002; Poulet and Petersen, 2008) and an in vitro model (Maier et al., 2009) to study synaptic input onto CA1 pyramidal cells during hippocampal ripples. We found that PSCs are phase-locked to ripples and coherent among
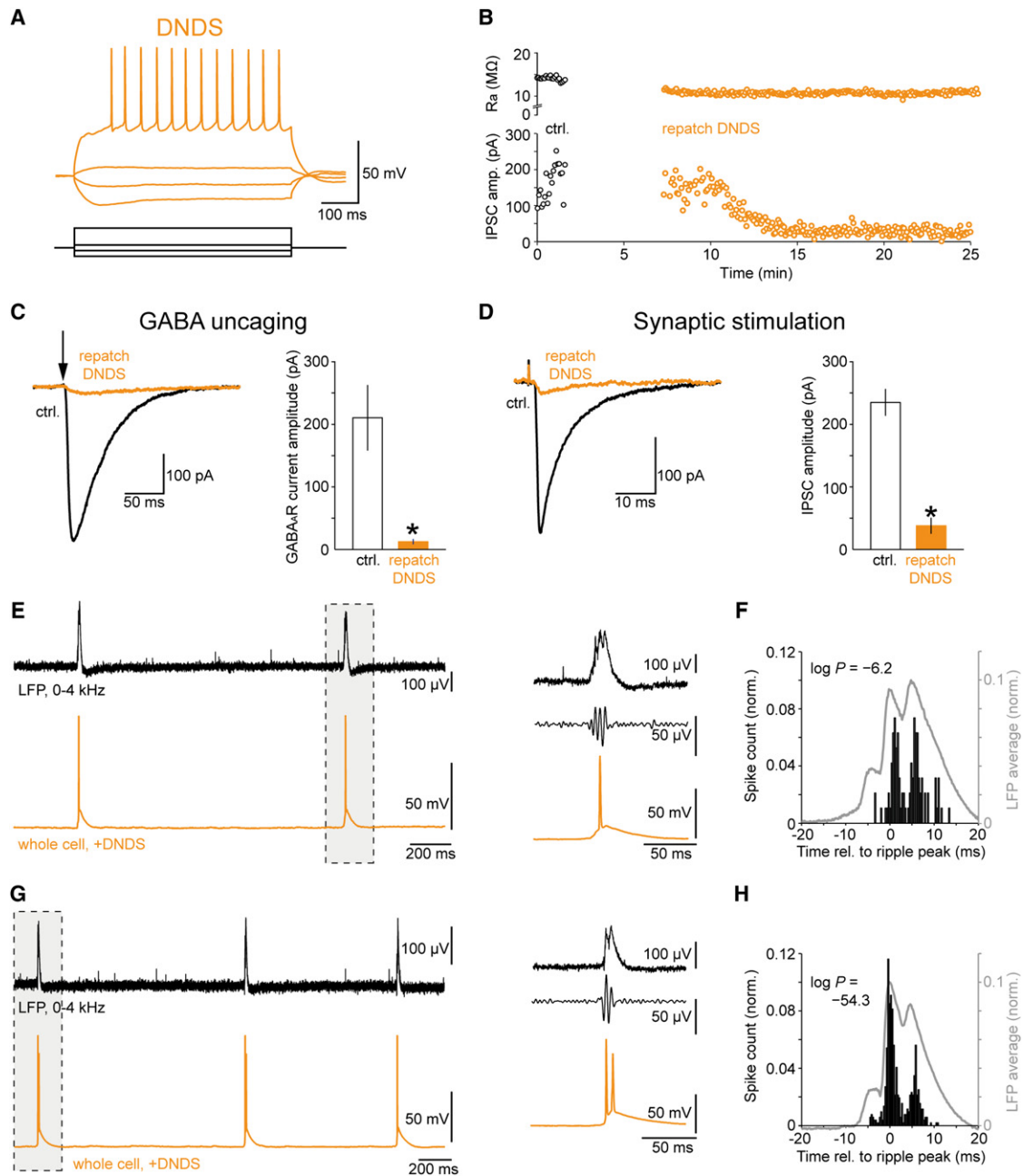
Figure 8. CA1 Pyramidal Cell Spiking Is Locked to Ripples when Inhibition Is Blocked at the Single-Cell Level

(A–D) Recordings with intracellular pipette solution containing the Cl⁻channel blocker DNDS.

(A) Input/response example in a CA1 pyramidal cell. De- and hyperpolarizing current steps were applied at +280 pA, ±40 pA, and −120 pA.

(B) Representative experiment to assess the potency of DNDS to block IPSCs. Upon a brief control period (black) in which IPSCs were elicited with synaptic stimulation, the electrode was withdrawn (AMPA, NMDA, and GABA$_B$ receptors blocked). The same cell was repatched (orange) with pipette solution containing 500 μM DNDS. After ∼5–10 min, IPSCs gradually decreased (lower panel); the cell's access resistance was monitored during the experiment (top panel).

(C) GABA uncaging experiments. UV-flash-evoked GABA currents were compared in the absence and presence of 500 μM DNDS. On average, DNDS reduced GABA currents by 93.8% ± 3.5% (control: 210.4 ± 52.4 pA versus DNDS: 12.4 ± 4.3 pA; mean ± SEM; n=5 repatch experiments; p = 0.008; two-tailed rank-sum test).

(D) DNDS effect on stimulus-induced IPSCs. Left: Example traces; right: population result; control: 234.9 ± 21.4 pA versus DNDS: 37.9 ± 12.9 pA (mean ± SEM; n=7 repatch experiments; p = 0.0006; two-tailed rank-sum test).

(E–H) Pyramidal neurons in CA1 were recorded in the current-clamp configuration during SWRs and slightly depolarized to enhance the spiking probability.

(E and G) Left: Two 120–300 Hz ripple-band-filtered representative experiments where cells displayed single or double spikes associated with SWRs. Right: Magnification of the boxed periods. Top: LFP; middle: ripple-band-filtered LFP; bottom: intracellular voltage trace.
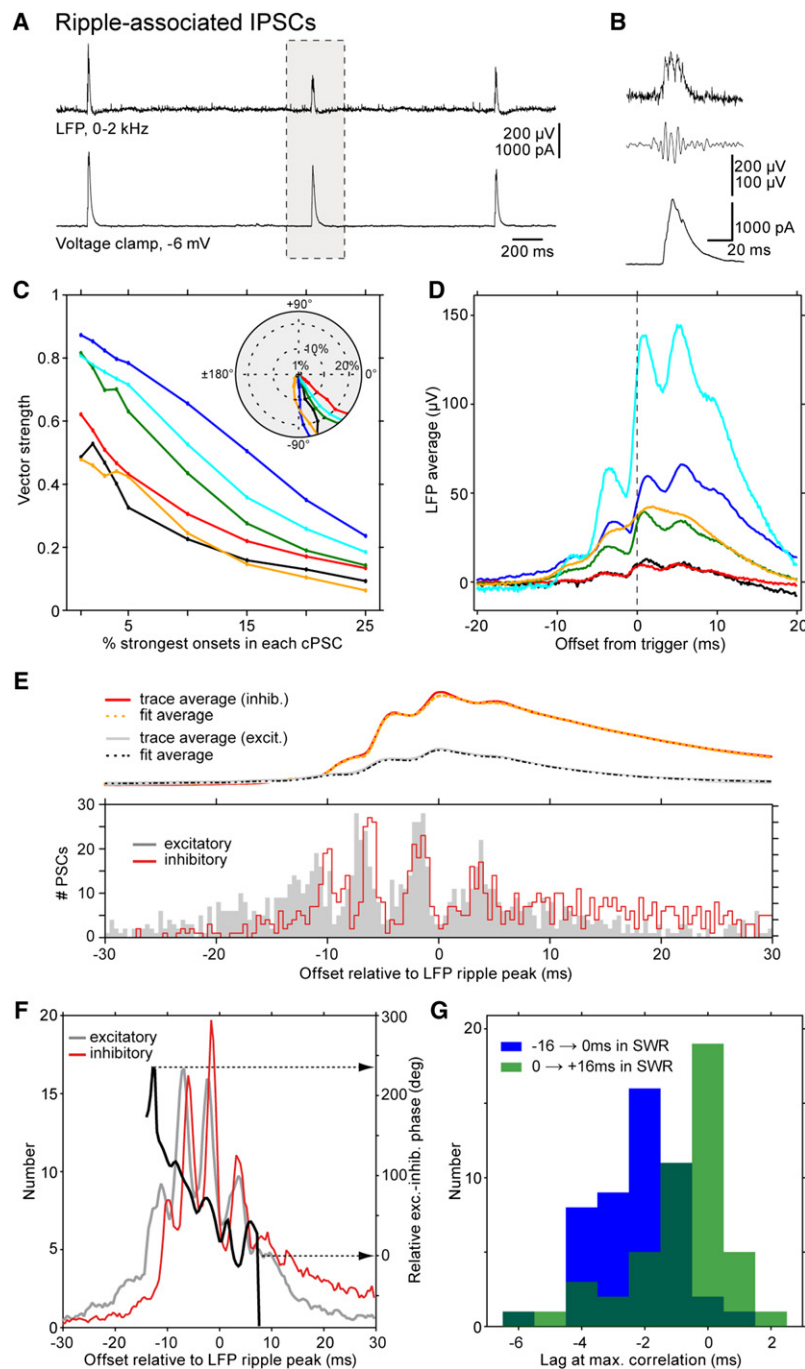
Figure 9. Analysis of Inhibitory Postsynaptic Currents during Ripples

(A) Inhibitory postsynaptic currents during SWRs were recorded at the reversal potential of excitation (−6 mV; Figure S8). SWRs (upper trace) are regularly associated with compound IPSCs (cIPSCs).

(B) Magnification of the event marked in (A). Top: wide-band signal (0–2 kHz); middle: 120–300 Hz filtered version of the above; bottom: cIPSC recorded in the voltage-clamp configuration.

(C) Vector strength of upward slopes versus fraction of strongest slopes (in respective individual cPSCs), indicating significant locking to ripple phase (p < 0.05; Rayleigh test) almost independent of the fraction of slopes taken into account. Colors identify individual cells. Inset: Polar plot of mean phases of cIPSCs for six experiments (colors) versus percent fraction of strongest slopes. Mean phase over cells at 10% threshold of strongest slopes is −60° ± 13°, corresponding to cIPSCs leading the LFP ripple peak by ~0.8 ms.

(D) cIPSCs lock to ripples, as demonstrated by averaging 40 ms LFP data stretches centered to cIPSC steepest upward slopes. Data from six cells using the 10% steepest slopes as trigger times (colors as in C).

(E) Peeling reconstruction of cIPSCs was used to infer IPSC onset times. Top: Mean reconstructed trace (orange) from a single-cell recording versus average recorded trace (red). An example of cEPSCs is shown inverted for comparison (gray, black). Bottom: Onset histogram of IPSCs and EPSCs from top. Initially, excitation and inhibition are phase-shifted with excitation leading inhibition by ~2 ms. Toward the end of the SWR, the two components come in phase.

(F) Averaged histograms of excitatory (8 cells; gray) and inhibitory onsets (6 cells; red). The local Hilbert phase difference among the two histograms (black) demonstrates a progressive reduction of the phase lag of inhibitory and excitatory onsets.

(G) Peak-correlation lag histograms derived from excitatory and inhibitory onset histograms (as in E). Inhibition follows excitation by ~1.5 ms early in the ripple (blue) but aligns later in the oscillation (green). Each count represents a combination of one excitatory and one inhibitory cell out of a total number of 48 combinations.

See also Figure S8.

those of non-SPW-associated EPSCs observed at the same holding potential. These phasic PSCs persisted after intracellular block of Cl⁻-mediated inhibition, thereby unequivocally demonstrating phasic, oscillation-coherent excitation during ripples. Block of inhibition at the single-cell level further revealed that ripple-locked excitation can regulate spike timing. Experiments in minislices devoid of the CA3 and subicular subfields demonstrated that ripple-coherent excitatory cPSCs can emerge locally within the CA1 network in vitro. Finally, ripple-associated excitatory and

principal neurons. These currents contained strong excitatory components: First, they could be observed at a membrane voltage with low driving force for Cl⁻, i.e., a recording condition for which GABA_A receptor-mediated synaptic inhibition is negligible. Further, kinetics of these currents were consistent with

(F and H) Spike-time histograms (black) of the two example cells demonstrate phase-locking of spikes and LFP SWRs (gray; averaged and normalized). Indicated log₁₀ p values represent the significance levels determined by the Rayleigh test. Log₁₀ p values in five other recordings were −1.6, −1.7, −2.6, −11.4, and −17.1. See also Figure S7.

inhibitory currents express an exquisite temporal precision and converge in phase.

Our results challenge the prevailing view that sharp-wave-associated ripples are shaped by phasic synaptic inhibition alone. This view is based on two experimental strategies of tackling ripple mechanisms in vivo: First, using sharp microelectrode recordings on CA1 pyramidal cells in anesthetized rats, Ylinen et al. (1995) varied the pipette Cl⁻ concentration and showed that ripple-associated postsynaptic potentials displayed phase shifts as expected from inhibitory PSPs. Second, extracellular recordings in vivo revealed that somatically targeting interneurons increase their discharge rate during ripples and fire rhythmically with the network oscillation (Csicsvari et al., 1999a). This finding has been confirmed more recently by juxtacellular recordings with post hoc morphological reconstructions, demonstrating that ripple-locked firing occurs in somatically targeting basket cells in anesthetized animals (Klausberger et al., 2003). Although our in vivo and in vitro recordings do corroborate the involvement of inhibition during ripples (see Figure S1B and Figure 9), our study adds that phasic excitatory inputs at ~200 Hz are also prominent during ripples and effective in regulating spike timing, as demonstrated by ripple-locked spiking when inhibition is blocked at the single-cell level (Figure 8).

Two possible sources of ripple-coherent EPSCs are conceivable: First, they could represent input from synaptically coupled CA3 pyramidal neurons. Indeed, phase coupling of CA3 pyramidal cell spikes with CA1 field ripples has been demonstrated (Both et al., 2008). However, our minislice data rule out this possibility as the only origin of ripple-locked EPSCs (Figure 7). Moreover, it has been demonstrated in vivo that CA3 cells do not discharge in phase with ripples recorded in CA1 (Csicsvari et al., 1999b; Sullivan et al., 2011). Another previous in vivo study showed that CA1 ripples persisted after CA3 input onto CA1 had been interrupted, although these surviving "mutant" ripples displayed lower oscillation frequency on average (Nakashiba et al., 2009). However, mutant ripples that fell into the control ripple frequency band were associated with unaltered spiking activity during ripples compared to the control condition with intact CA3 input (their Figure 3F). It is not clear, though, which signal was the immediate trigger for the CA1 network to generate mutant ripples. Feasible inputs might arise from entorhinal cortex or thalamus (Nakashiba et al., 2009). Collectively, though Schaffer collateral input onto CA1 may be obligatory for the transfer of information involved in memory consolidation, transmission from CA3 to CA1 does not seem to be required for the occurrence of ripple oscillations in CA1 (see also Buzsáki et al., 1992).

Ripple-coherent EPSCs in CA1 minislices are consistent with a second framework to explain their origin. In this scenario, these currents are assumed to be of purely local emergence, resulting from recurrent synaptic input alone (Deuchars and Thomson, 1996).

Cellular processes involved in triggering sharp waves are still subject to investigations. Recently, it has been proposed that sharp waves in CA3 may be induced by rebound depolarization following strong inhibitory activity (Ellender et al., 2010). Sharp-wave-associated excitation arriving from CA3 (Buzsáki, 1986) may consequently trigger sharp waves in CA1, which secondarily give rise to ripples.

The mechanisms responsible for the generation and maintenance of ripples are also a matter of debate. Computational network models provide two possible explanations: First, ripples may reflect the synchronous discharge of pyramidal cells during the replay of memory sequences (as formulated for CA3 by Leibold and Kempter, 2006). Alternatively, electrical coupling of CA1 principal cell axons may generate oscillations in the ripple frequency range (Traub et al., 1999; Traub and Bibbig, 2000). This latter hypothesis is supported by experimental reports of spikelets being a consequence of electrical coupling between axons of cortical pyramidal neurons (Draguhn et al., 1998; Schmitz et al., 2001; Wang et al., 2010). Along this line, recent work has demonstrated bursts of spikelets in the hippocampus during behavior in vivo (Harvey et al., 2009) and even at ripple frequency (Epsztein et al., 2010). The observed ripple-locked EPSCs could thus correspond to rhythmic output of a gap junction-coupled network of CA1 principal cells. Consistent with this possibility, SWR incidence and cPSC ripple-band power were reduced following application of carbenoxolone (CBX; Figure S9A). However, in agreement with previous work (Tovar et al., 2009), CBX also weakened both excitatory and inhibitory synaptic transmission in our experimental system (Figures S9B and S9C). In light of the poor specificity of CBX, a known limitation of gap junction blockers in general, the hypothesized role of gap junctions in synchronizing the axonal network during ripples remains unsettled and has to be addressed in future work.

In summary, we demonstrated coherent excitatory currents in CA1 pyramidal neurons during ripples. These oscillation-locked inputs represent synchronous activity of assemblies of principal cells as has been proposed in several in vivo and modeling studies (Dragoi and Tonegawa, 2011; Harris et al., 2003; Leibold and Kempter, 2006; O'Neill et al., 2008; Wilson and McNaughton, 1994).

EXPERIMENTAL PROCEDURES

Ethics Statement
Animal maintenance and experiments were in accordance with the respective guidelines of local authorities (Berlin state government, T0100/03 and G188-09) and followed the German animal welfare act and the European Council Directive 86/609/EEC on protection of animals used for experimental and other scientific purposes.

Animal Surgery and Electrophysiology In Vivo
All in vivo experimental procedures followed previously described methods (Crochet and Petersen, 2006; Poulet and Petersen, 2008). Male 3- to 6-week-old C57Bl/6 mice were anesthetized and implanted with a light-weight metal head holder. After surgery, animals were allowed to recover for at least 1 day before habituation to head restraint started. Habituation was repeated for several days until the animal sat calmly for a period of 1–2 hr. On the day of the experiment, two small craniotomies, for LFP and whole-cell recordings, were made under isoflurane anesthesia (1.5%). Animals were then allowed to recover for at least 2 hr before recordings started. Coordinates for craniotomies were determined stereotactically on the left hemisphere: 2 or 3 mm, respectively, posterior of bregma, and 2 mm lateral of the midline.

For LFP recordings, we used glass pipettes (5–7 MΩ) filled with Ringer's solution. To determine the recording depth of the area of interest (i.e., CA1

stratum pyramidale), LFP electrodes in both craniotomies were lowered slowly until clear ripple activity was detected, usually at about 1200–1300 μm depth. Then one pipette was retracted and replaced by a patch pipette. Whole-cell recordings were made with 5–7 MΩ glass electrodes filled with intracellular solution containing (in mM): 135 K-gluconate, 4 KCl, 4 MgATP, 10 Na$_2$phosphocreatine, 0.3 Na$_3$GTP, 10 Hepes (pH adjusted to 7.3 with KOH; 2 mg/ml biocytin). The liquid junction potential was accounted for by subtracting 7 mV from all recorded voltages (Lee et al., 2009). On average, the initial resting membrane potential of these neurons was −61.8 ± 1.4 mV, and the mean action potential amplitude was 47.1 ± 3.5 mV (12 cells). All in vivo signals were amplified 100× with a Multiclamp 700B (Axon Instruments, Union City, CA, USA), filtered at 10 kHz, digitized at 20 kHz (ITC-18; HEKA Elektronik, Lambrecht, Germany), and stored (IgorPro; WaveMetrics, Lake Oswego, OR, USA).

Slice Preparation and Electrophysiology In Vitro
Horizontal slices (400 μm) were prepared from ventral to mid-hippocampus of C57Bl/6 mice 4 to 8 weeks old, and slices were maintained at the surface of oxygenated artificial cerebrospinal fluid (ACSF) at ∼35°C. ACSF contained (in mM): 119 NaCl, 2.5 KCl, 1.3 MgCl$_2$, 2.5 CaCl$_2$, 10 glucose, 1 NaH$_2$PO$_4$, 26 NaHCO$_3$. Osmolarity of ACSF was routinely checked (290–310 mosmol/l). Slices were incubated for 1–4 hr before being transferred to a submerged chamber for recordings at ∼32°C.

Data were recorded in Igor Pro using a Multiclamp 700A amplifier. Extracellular LFPs were recorded with ACSF-filled glass electrodes (resistance: 0.2–0.3 MΩ). Signals were amplified 1000×, low-pass filtered at 2 kHz or 4 kHz, and digitized at 5 kHz or 10 kHz. Whole-cell recordings were performed with borosilicate glass electrodes (2–5 MΩ) filled with one of the following intracellular solutions (in mM): (1) 120 K-gluconate, 10 KCl, 10 HEPES, 5 EGTA, 3 MgATP, 2 MgSO$_4$, 1 GTP; (2) CsF-DIDS solution: 120 Cs-fluoride, 10 KCl, 10 HEPES, 5 EGTA, and 1 4,4′-diisothiocyanatostilbene-2,2′-disulfonic acid (DIDS); (3) for DNDS experiments: 70 K-gluconate, 45 KCl, 5 CaCl$_2$, 10 HEPES, 4 MgATP, 0.4 NaGTP, 5 phosphocreatine, 500 μM 4,4′-dinitrostilbene-2,2′-disulfonic acid, disodium salt (DNDS); The pH of solutions 1 to 3 was adjusted to ∼7.4 with KOH; (4) Cs-based intracellular solution contained (mM) 120 gluconic acid, 10 KCl, 2 MgSO$_4$, 3 MgATP, 1 NaGTP, 5 EGTA, 10 HEPES; pH adjusted to ∼7.4 with 1 M CsOH. In the whole-cell current-clamp configuration, de- and hyperpolarizing current steps (200–1000 ms) were applied to characterize the cell's intrinsic properties; only cells that showed typical spiking characteristics of principal cells were considered. Series resistance (R$_s$) was monitored continuously throughout experiments; cells were rejected if R$_s$ exceeded 20 MΩ or varied >30% during recordings. No R$_s$ compensation was used. Voltages were liquid junction potential-corrected (experimentally determined; Neher, 1992).

GABA Uncaging
Caged GABA (20 ml at 100 μM) was reperfused at 2.5–3.0 ml/min. Uncaging was done using a UV-pulsed laser (Rapp OptoElectronic, Wedel, Germany) attached with a 200 μm optical fiber coupled into the epifluorescence port of the microscope with an OSI-BX adaptor (Rapp OptoElectronic) and focused on the specimen by the objective lens. This yielded an illuminated circle of 20–50 μm. Laser flash duration was 5 ms. Laser power under the objective corresponding to the stimulus intensity levels used was monitored with a photodiode array-based photodetector (PDA-K-60, Rapp OptoElectronic) and did not change over time. GABA was uncaged over the cell soma in the presence of 10 μM NBQX and 50 μM APV.

Anatomical Reconstruction
Cells were routinely loaded with 0.3%–0.5% biocytin. After recording, slices were transferred to a fixative solution containing 4% paraformaldehyde (PFA) and 0.2% saturated picric acid in 0.1 M phosphate buffer. For in vivo experiments, mice were deeply anesthetized (urethane) immediately after the experiment and perfused with 4% PFA. After overnight fixation, brains were cut into 100 μm thick coronal slices. Biocytin-filled cells were subsequently visualized with 3,3′-diaminobenzidine tetrahydrochloride (0.015%) using a standard ABC kit (Vectorlabs, Burlingame, CA, USA) and reconstructed on a light microscope at 40× with a Neurolucida 3D system (MicroBrightField, Williston, VT, USA).

Applied Drugs
2,3-dioxo-6-nitro-1,2,3,4-tetrahydrobenzo(f)quinoxaline-7-sulfonamide (NBQX), DIDS, and caesium fluoride were purchased from Sigma Aldrich, Germany. 6-Imino-3-(4-methoxyphenyl)-1(6H)-pyridazinebutanoic acid hydrobromide (gabazine) and D-(-)-2-Amino-5-phosphonopentanoic acid (D-APV) were obtained from Biotrend, Cologne, Germany. γ-aminobutyric acid, α-carboxy-2-nitrobenzyl ester, trifluoroacetic acid salt (O-(CNB-caged) GABA) was purchased from Molecular Probes (Eugene, OR, USA). DNDS was kindly provided by Dr. Robert J. Bridges, Rosalind Franklin University of Medicine and Science, Chicago, IL, USA.

Data Analysis
We analyzed the data using either Matlab (The Mathworks, Natick, MA, USA) or Python 2.6.5 with the modules Numpy 1.5.0 and Scipy 0.8.0. The Rayleigh test was run under R 2.10.1 using the package circular 0.3-8.

Identification of SWRs and Postsynaptic Activity In Vivo
SWRs in vivo were detected with custom-made Matlab code similar to procedures described previously (Csicsvari et al., 1999a) (Figure S1). LFP data were bandpass-filtered at 120–300 Hz and rectified. After smoothing with a sliding average filter (10 ms window size), peaks were identified whose maxima exceeded a threshold set to 6× the standard deviation (SD) of eventless LFP data (noise). Events with durations <12 ms at 2×SD of noise were discarded. Within the individual LFP ripple, the maximum positive ripple deflection was taken as a time reference, and 400 ms stretches of extra- and intracellular traces centered to this reference were cut out and stored for analysis.

In Vitro Sharp-Wave and cPSC Identification
SWRs were selected using an amplitude-based criterion. The algorithm described below was validated by visual inspection with an emphasis on avoiding false positives rather than false negatives. In detail, SWR detection was performed on 4–100 Hz bandpass-filtered extracellular traces (2nd order zero-phase, acausal Butterworth filter). Their amplitudes were tallied, and the resulting amplitude histogram was fitted with a Gaussian that was dominated by the eventless epochs of small amplitude. The tails provided us with an expected frequency of rare events. We found the threshold as the lowest amplitude, which appeared 500 times more often than expected from the Gaussian fit of amplitudes. Any signal above threshold was accepted as an SWR event if it was surrounded by at least 7 ms more of suprathreshold activity in a 150 ms time window centered on it. The SWR maximum in such a window was used to locate cPSCs in the voltage-clamp trace.

Spectral Content of SWRs
Spectral content of SWRs was analyzed in 100 ms stretches of raw data centered on the SWR peak, using the Fast Fourier Transform (FFT). Frequency resolution of the resulting power spectral density (PSD) plots was 9.98 Hz.

Slope Analysis of Postsynaptic Currents
PSCs are characterized by a steep onset phase followed by a gentler decay (see Figure 4A for the separation of timescales). The initial sharp deflection can be used as a proxy for the onset itself. To select steep slopes (Figure 4B, inset), we smoothed cPSC traces in 80 ms windows around the SWR maxima (Butterworth order 2 zero-phase filter 0.5–400 Hz; black trace) and calculated the extrema of their time derivative (gray trace). This procedure marks slopes both in the onset and in the decay of PSCs. From the kinetic information obtained for isolated PSCs, the former are expected to be steeper even when several time-shifted PSCs overlap. The values of the derivative at such extremal points are shown as cumulative histograms in Figures 4B and 6D.

We found that for our data, FFT does not allow quantitative statements on the fast structure of cPSCs because of their short duration and the disproportionate weight assigned to events with higher-amplitude oscillations. Also, the temporal fine structure differs from event to event. This variability is particularly problematic for analyses in the frequency domain, as for high frequencies f a small temporal jitter Δt is transformed to a large frequency jitter $\Delta f = -f^2/\Delta t$ owing to the reciprocal relation $f = 1/t$. To quantify the rhythmicity

of fast network input during cPSCs, we instead analyzed the intervals between strong slopes within cPSCs (Figure 4C: 10% strongest interdownward slope intervals in red, 25% strongest in gray; 0.5–400 Hz trace; see also Figures 6E and S4B). The ripple band peak is robust for a wide range of low-pass frequencies (400–600 Hz) and fractions of selected strongest slopes (1%–25%). Filtering out higher frequencies is required to avoid too many local extrema of the derivatives being detected for what is in practice the same onset.

Identification of Non-SWR-Associated PSCs and Their Kinetics

EPSCs outside SWRs ("spontaneous PSCs") were detected among the cells recorded at −66 mV as strong downward slopes (top 5% of all maximal slopes on the 0.5–400 Hz filtered intracellular trace of each cell). A total of 1,000 events from 5 cells were postselected by eye to exclude those that are too small to be distinguished from noise and also to avoid multiple events where a second PSC arrives during the tail of the first.

The fit was performed with an alpha function

$$\alpha(t;\ A,\ t_0,\ \tau_\mathrm{d},\ \tau_\mathrm{r}) = A N(\tau_\mathrm{d},\ \tau_\mathrm{r}) \Theta(t - t_0) \left[\mathrm{e}^{-\frac{(t-t_0)}{\tau_\mathrm{d}}} - \mathrm{e}^{-\frac{(t-t_0)}{\tau_\mathrm{r}}} \right],$$

where $N(\tau_\mathrm{d},\tau_\mathrm{r})$ is a normalization factor so that the fitted amplitude A corresponds to the maximum value attained by the function, and $\Theta(t-t_0)$ is the Heaviside step function defined as 1 for positive arguments (t later than onset t_0) and 0 elsewhere. The average time constants obtained from the fits were of $\tau_r = 1.70 \pm 0.04$ ms and $\tau_d = 4.04 \pm 0.08$ ms. Here our PSC detection algorithm is based on slopes that are influenced by both time constants. To highlight the separation of timescales used by the algorithm, we plot histograms of durations of rises and decays (20%–80% and 80%–20% of maximum amplitude) instead of time constants (Figure 4A).

Locking of Intracellular cPSCs to Extracellular Ripple

We provide three measures of temporal coordination between intra- and extracellular signals during SWRs: (1) coherence, demonstrating synchronization of both signals at ripple frequency; (2) slope-triggered SWR averages showing the alignment of the intracellular strong downward slopes with a particular phase of the extracellular ripple oscillation; and (3) vector strength, which quantifies the magnitude of the effect as a function of the threshold for slope selection.

Coherence

The coherence $C_{xy}(f)$ of two signals x and y is defined as their normalized cross-spectral density. For a given frequency f, the coherence is higher the more stable the phase difference of the signals:

$$C_{xy} = \frac{|P_{xy}|^2}{P_x P_y}.$$

Coherence was computed using PSDs by the Welch periodogram method with 256 FFT points.

Slope-Triggered Averages of SWRs

Slope-triggered averages (Figures 4D and 9D) were computed by averaging windows of 40 ms LFP data centered to the times of strongest 10% slopes of each cPSC. Ripple modulation of the resulting averages indicates a consistent phase of the putative EPSC onsets (or putative IPSC onsets, Figure 9D) in the oscillation defined by the extracellular ripple. The presence of the bulk of the signal after the onset (0 ms offset) indicates a tendency for stronger slopes to concentrate at the beginning of the cPSC. cPSCs with only one strong slope were removed from the analysis. For the analysis shown in Figure 4, a total of 1,085 cPSCs were represented with 5,161 onsets, each cell having an average of 4 to 5 onsets per cPSC. For the complementary analysis presented in Figure 9, a total of 849 cPSCs from 6 cells were represented with 3,037 onsets, each cell showing an average of 3 to 5 onsets per cPSC.

Vector Strength

To assign phases with respect to the ripple component of the LFP, we applied a Hilbert transform on the 120–300 Hz-filtered extracellular potential. Each putative EPSC event (or putative IPSC event, Figure 9D) detected by its extremal slope was assigned a Hilbert phase, ϕ_j. As an indicator for locking quality of these collected EPSC (or IPSC) phases, we use the vector strength (VS) or mean resultant length, which is normalized between 0 and 1:

$$\mathrm{VS}(\phi) = \frac{1}{N} \left| \sum_{j=1}^{N} \mathrm{e}^{-\mathrm{i}\phi_j} \right|.$$

Figures 4E and 9C illustrate the dependence of vector strength and phase (polar plots in insets) as a function of the slope threshold used for EPSC (or IPSC) detection (in the range of 1% to 25%). All vector strengths and phases plotted are significant according to a Rayleigh test for the uniformity of a phase distribution with p < 0.05.

Statistical Analysis

Data are presented as means ± standard error of the mean (SEM), unless otherwise stated. Statistical significance was assessed using Wilcoxon's rank-sum test, the two-sample Kolmogorov-Smirnov test, or the Rayleigh test for circular statistics. Statistical significance was indicated at the given level (p) with $\alpha = 0.05$ regarded significant, unless otherwise designated.

SUPPLEMENTAL INFORMATION

Supplemental Information includes Supplemental Experimental Procedures and nine figures and can be found with this article online at doi:10.1016/j.neuron.2011.08.016.

REFERENCES

Axmacher, N., Elger, C.E., and Fell, J. (2008). Ripples in the medial temporal lobe are relevant for human memory consolidation. Brain 131, 1806–1817.

Both, M., Bähner, F., von Bohlen und Halbach, O., and Draguhn, A. (2008). Propagation of specific network patterns through the mouse hippocampus. Hippocampus 18, 899–908.

Buzsáki, G. (1986). Hippocampal sharp waves: their origin and significance. Brain Res. 398, 242–252.

Buzsáki, G. (1989). Two-stage model of memory trace formation: a role for "noisy" brain states. Neuroscience 31, 551–570.

Buzsáki, G., Horváth, Z., Urioste, R., Hetke, J., and Wise, K. (1992). High-frequency network oscillation in the hippocampus. Science 256, 1025–1027.

Buzsáki, G., Buhl, D.L., Harris, K.D., Csicsvari, J., Czéh, B., and Morozov, A. (2003). Hippocampal network patterns of activity in the mouse. Neuroscience 116, 201–211.

Carr, M.F., Jadhav, S.P., and Frank, L.M. (2011). Hippocampal replay in the awake state: a potential substrate for memory consolidation and retrieval. Nat. Neurosci. 14, 147–153.

Crochet, S., and Petersen, C.C. (2006). Correlating whisker behavior with membrane potential in barrel cortex of awake mice. Nat. Neurosci. 9, 608–610.

Csicsvari, J., Hirase, H., Czurkó, A., Mamiya, A., and Buzsáki, G. (1999a). Oscillatory coupling of hippocampal pyramidal cells and interneurons in the behaving Rat. J. Neurosci. 19, 274–287.

Csicsvari, J., Hirase, H., Czurkó, A., Mamiya, A., and Buzsáki, G. (1999b). Fast network oscillations in the hippocampal CA1 region of the behaving rat. J. Neurosci. *19*, RC20.

Csicsvari, J., O'Neill, J., Allen, K., and Senior, T. (2007). Place-selective firing contributes to the reverse-order reactivation of CA1 pyramidal cells during sharp waves in open-field exploration. Eur. J. Neurosci. *26*, 704–716.

Deuchars, J., and Thomson, A.M. (1996). CA1 pyramid-pyramid connections in rat hippocampus in vitro: dual intracellular recordings with biocytin filling. Neuroscience *74*, 1009–1018.

Diekelmann, S., and Born, J. (2010). The memory function of sleep. Nat. Rev. Neurosci. *11*, 114–126.

Dragoi, G., and Tonegawa, S. (2011). Preplay of future place cell sequences by hippocampal cellular assemblies. Nature *469*, 397–401.

Draguhn, A., Traub, R.D., Schmitz, D., and Jefferys, J.G. (1998). Electrical coupling underlies high-frequency oscillations in the hippocampus in vitro. Nature *394*, 189–192.

Dudek, S.M., and Friedlander, M.J. (1996). Intracellular blockade of inhibitory synaptic responses in visual cortical layer IV neurons. J. Neurophysiol. *75*, 2167–2173.

Ego-Stengel, V., and Wilson, M.A. (2010). Disruption of ripple-associated hippocampal activity during rest impairs spatial learning in the rat. Hippocampus *20*, 1–10.

Eichenbaum, H. (2000). A cortical-hippocampal system for declarative memory. Nat. Rev. Neurosci. *1*, 41–50.

Ellender, T.J., Nissen, W., Colgin, L.L., Mann, E.O., and Paulsen, O. (2010). Priming of hippocampal population bursts by individual perisomatic-targeting interneurons. J. Neurosci. *30*, 5979–5991.

Epsztein, J., Lee, A.K., Chorev, E., and Brecht, M. (2010). Impact of spikelets on hippocampal CA1 pyramidal cell activity during spatial exploration. Science *327*, 474–477.

Girardeau, G., Benchenane, K., Wiener, S.I., Buzsáki, G., and Zugaro, M.B. (2009). Selective suppression of hippocampal ripples impairs spatial memory. Nat. Neurosci. *12*, 1222–1223.

Harris, K.D., Csicsvari, J., Hirase, H., Dragoi, G., and Buzsáki, G. (2003). Organization of cell assemblies in the hippocampus. Nature *424*, 552–556.

Harvey, C.D., Collman, F., Dombeck, D.A., and Tank, D.W. (2009). Intracellular dynamics of hippocampal place cells during virtual navigation. Nature *461*, 941–946.

Ji, D., and Wilson, M.A. (2007). Coordinated memory replay in the visual cortex and hippocampus during sleep. Nat. Neurosci. *10*, 100–107.

Jinno, S., Klausberger, T., Marton, L.F., Dalezios, Y., Roberts, J.D., Fuentealba, P., Bushong, E.A., Henze, D., Buzsáki, G., and Somogyi, P. (2007). Neuronal diversity in GABAergic long-range projections from the hippocampus. J. Neurosci. *27*, 8790–8804.

Johnson, A., and Redish, A.D. (2007). Neural ensembles in CA3 transiently encode paths forward of the animal at a decision point. J. Neurosci. *27*, 12176–12189.

Karlsson, M.P., and Frank, L.M. (2009). Awake replay of remote experiences in the hippocampus. Nat. Neurosci. *12*, 913–918.

Klausberger, T., Magill, P.J., Márton, L.F., Roberts, J.D., Cobden, P.M., Buzsáki, G., and Somogyi, P. (2003). Brain-state- and cell-type-specific firing of hippocampal interneurons in vivo. Nature *421*, 844–848.

Klausberger, T., Márton, L.F., Baude, A., Roberts, J.D., Magill, P.J., and Somogyi, P. (2004). Spike timing of dendrite-targeting bistratified cells during hippocampal network oscillations in vivo. Nat. Neurosci. *7*, 41–47.

Klausberger, T., Márton, L.F., O'Neill, J., Huck, J.H., Dalezios, Y., Fuentealba, P., Suen, W.Y., Papp, E., Kaneko, T., Watanabe, M., et al. (2005). Complementary roles of cholecystokinin- and parvalbumin-expressing GABAergic neurons in hippocampal network oscillations. J. Neurosci. *25*, 9782–9793.

Kudrimoti, H.S., Barnes, C.A., and McNaughton, B.L. (1999). Reactivation of hippocampal cell assemblies: effects of behavioral state, experience, and EEG dynamics. J. Neurosci. *19*, 4090–4101.

Lansink, C.S., Goltstein, P.M., Lankelma, J.V., McNaughton, B.L., and Pennartz, C.M. (2009). Hippocampus leads ventral striatum in replay of place-reward information. PLoS Biol. *7*, e1000173.

Lee, A.K., and Wilson, M.A. (2002). Memory of sequential experience in the hippocampus during slow wave sleep. Neuron *36*, 1183–1194.

Lee, A.K., Manns, I.D., Sakmann, B., and Brecht, M. (2006). Whole-cell recordings in freely moving rats. Neuron *51*, 399–407.

Lee, A.K., Epsztein, J., and Brecht, M. (2009). Head-anchored whole-cell recordings in freely moving rats. Nat. Protoc. *4*, 385–392.

Leibold, C., and Kempter, R. (2006). Memory capacity for sequences in a recurrent network with biological constraints. Neural Comput. *18*, 904–941.

Maier, N., Nimmrich, V., and Draguhn, A. (2003). Cellular and network mechanisms underlying spontaneous sharp wave-ripple complexes in mouse hippocampal slices. J. Physiol. *550*, 873–887.

Maier, N., Morris, G., Johenning, F.W., and Schmitz, D. (2009). An approach for reliably investigating hippocampal sharp wave-ripples in vitro. PLoS ONE *4*, e6925.

Margrie, T.W., Brecht, M., and Sakmann, B. (2002). In vivo, low-resistance, whole-cell recordings from neurons in the anaesthetized and awake mammalian brain. Pflugers Arch. *444*, 491–498.

Nakashiba, T., Buhl, D.L., McHugh, T.J., and Tonegawa, S. (2009). Hippocampal CA3 output is crucial for ripple-associated reactivation and consolidation of memory. Neuron *62*, 781–787.

Neher, E. (1992). Correction for liquid junction potentials in patch clamp experiments. Methods Enzymol. *207*, 123–131.

Nelson, S., Toth, L., Sheth, B., and Sur, M. (1994). Orientation selectivity of cortical neurons during intracellular blockade of inhibition. Science *265*, 774–777.

Nimmrich, V., Maier, N., Schmitz, D., and Draguhn, A. (2005). Induced sharp wave-ripple complexes in the absence of synaptic inhibition in mouse hippocampal slices. J. Physiol. *563*, 663–670.

O'Keefe, J. (1976). Place units in the hippocampus of the freely moving rat. Exp. Neurol. *51*, 78–109.

O'Keefe, J., and Nadel, L. (1978). The Hippocampus as a Cognitive Map (Cambridge, UK: Oxford University Press).

O'Neill, J., Senior, T.J., Allen, K., Huxter, J.R., and Csicsvari, J. (2008). Reactivation of experience-dependent cell assembly patterns in the hippocampus. Nat. Neurosci. *11*, 209–215.

Poulet, J.F., and Petersen, C.C. (2008). Internal brain state regulates membrane potential synchrony in barrel cortex of behaving mice. Nature *454*, 881–885.

Schmitz, D., Schuchmann, S., Fisahn, A., Draguhn, A., Buhl, E.H., Petrasch-Parwez, E., Dermietzel, R., Heinemann, U., and Traub, R.D. (2001). Axo-axonal coupling. a novel mechanism for ultrafast neuronal communication. Neuron *31*, 831–840.

Siapas, A.G., and Wilson, M.A. (1998). Coordinated interactions between hippocampal ripples and cortical spindles during slow-wave sleep. Neuron *21*, 1123–1128.

Sullivan, D., Csicsvari, J., Mizuseki, K., Montgomery, S., Diba, K., and Buzsáki, G. (2011). Relationships between hippocampal sharp waves, ripples, and fast gamma oscillation: influence of dentate and entorhinal cortical activity. J. Neurosci. *31*, 8605–8616.

Tovar, K.R., Maher, B.J., and Westbrook, G.L. (2009). Direct actions of carbenoxolone on synaptic transmission and neuronal membrane properties. J. Neurophysiol. *102*, 974–978.

Traub, R.D., and Bibbig, A. (2000). A model of high-frequency ripples in the hippocampus based on synaptic coupling plus axon-axon gap junctions between pyramidal neurons. J. Neurosci. *20*, 2086–2093.

Traub, R.D., Schmitz, D., Jefferys, J.G., and Draguhn, A. (1999). High-frequency population oscillations are predicted to occur in hippocampal

pyramidal neuronal networks interconnected by axoaxonal gap junctions. Neuroscience *92*, 407–426.

Wang, Y., Barakat, A., and Zhou, H. (2010). Electrotonic coupling between pyramidal neurons in the neocortex. PLoS ONE *5*, e10253.

Wierzynski, C.M., Lubenov, E.V., Gu, M., and Siapas, A.G. (2009). State-dependent spike-timing relationships between hippocampal and prefrontal circuits during sleep. Neuron *61*, 587–596.

Williams, S.R., and Mitchell, S.J. (2008). Direct measurement of somatic voltage clamp errors in central neurons. Nat. Neurosci. *11*, 790–798.

Wilson, M.A., and McNaughton, B.L. (1994). Reactivation of hippocampal ensemble memories during sleep. Science *265*, 676–679.

Ylinen, A., Bragin, A., Nádasdy, Z., Jandó, G., Szabó, I., Sík, A., and Buzsáki, G. (1995). Sharp wave-associated high-frequency oscillation (200 Hz) in the intact hippocampus: network and intracellular mechanisms. J. Neurosci. *15*, 30–46.